Electronic Supplementary Material (ESI) for Journal of Materials Chemistry A.

Supplementary Information

Conversion of CO_2 to chemical feedstocks over bismuth nanosheets *in situ* grown on nitrogen-doped carbon

Xin Wang[a, #], Wen-Jin Yin[b, #], Yubing Si[a], Xiaoming Wang[a], Xiaoxiao Guo[a], Wei Guo[a] and Yongzhu Fu[a, *]

[a] College of Chemistry and Center of Green Catalysis, Zhengzhou University, Zhengzhou 450001, P. R. China
[b] School of Physics and Electronic Science, Hunan University of Science and Technology, Xiangtan 411201, P. R. China
[*] Correspondence author
E-mail: yfu@zzu.edu.cn (Yongzhu Fu)
Xin Wang (orcid.org/0000-0002-8965-4910)

Methods

Specifications of chemicals

$Bi(NO_3)_3 \cdot 5H_2O$, CH_4N_2Se, $LiOH \cdot H_2O$, $KHCO_3$, KOH (absolute GR, 99.7%) were purchased from Sinopharm Chemical Reagent Company. The commercial Bi nanopowder was purchased from Macklin (99.99%, 200 mesh). D_2O, 3-(Trimethylsilyl)-1-propanesulfonic acid sodium (DSS), ethanol (absolute GR, 99.7%), HCOOH (> 99.99%), CH_3OH (> 99.99%) were purchased from Alfa Aesar. N-doped ordered mesoporous carbon (OMC-N) was purchased from Nanjing XFNANO Materials Tech Co., Ltd. Super P was purchased from Guangdong Canrd New Energy Technology Co.,Ltd . Nafion perfluorinated ion-exchange resin solution (5 *wt.*% in mixture of lower aliphatic alcohol & H_2O) was all purchased from Sigma Aldrich. Nafion® N-117 membrane with a thickness of 0.18 mm was purchased from Alfa Aesar. Carbon fiber paper was obtained from FuelCell. All the chemicals were used without further purification. All the aqueous solutions were prepared with Milli Q water (18.2 MΩ cm).

Preparation of Bi_2O_2Se nanosheets and Bi_2O_2Se nanosheets grown on N-doped carbon

In a typical synthesis, ten milliliters of deionized water, 4 mmol of $Bi(NO_3)_3 \cdot 5H_2O$, and 2 mmol of CH_4N_2Se were added into a 50 mL beaker to form a yellow solution under stirring. Afterward, 12 g of $LiOH \cdot H_2O$ powder was added gradually into the beaker to form a black mixture under stirring for 10 min. Finally, the reaction mixture was then transferred into a 50 mL Teflon-lined stainless-steel autoclave. The crystallization process was carried out under autogenous pressure at 120 °C for 1 hour. After the autoclave was cooled and depressurized, the final products were taken out and poured into 40 mL of deionized water, and collected by centrifugation, repetitively washed with deionized water, and finally lyophilized. The semiconducting Bi_2O_2Se nanosheets with different sizes were synthesized under different conditions, which the specific synthesis conditions are listed in Table S1. For the synthesis of Bi_2O_2Se/OMC-N, it has same synthesis procedure except adding 0.2865 g N-doped ordered mesoporous carbon (OMC-N). The OMC-N was added into the beaker to form a black liquid under stirring after the addition of CH_4N_2Se. Afterward, the addition of lithium hydroxide and subsequent hydrothermal process was same as Bi_2O_2Se nanosheets.

Electroreduction of Bi_2O_2Se NSs and Bi_2O_2Se NSs/OMC-N

Preparation of slurry: 5 mg of Bi_2O_2Se and 2.5 mg of Super P were dispersed in 1 mL of ethanol with the addition of 100 μL of 5 *wt.*% Nafion, and vigorously sonicated for 40 min to form a homogenous ink. The slurry of Bi_2O_2Se NSs/OMC-N was prepared the same procedure with the above slurry except the adding of Super P. The commercial Bi nanopowder was purchased from Macklin (99.99%, 200 mesh). The slurry of Bi nanoparticles was prepared with 5 mg Bi nanopowder and 2.5 mg Super P. The slurries of Super P and OMC-N were prepared using the same procedure and concentration.

The slurry was dropcast onto a 1 × 1 cm^2 Teflon-treated carbon fiber paper (HCP020P, from HESEN AvCarb P75 from Fuel Cell Store) to reach areal loading of 1 mg cm^{-2} and naturally dried. Electrochemical experiments were carried out in a custom-designed gas-tight H-shaped electrochemical cell with two compartments separated by a piece of Nafion-117 proton exchange membrane as the separator. Carbon fiber paper modified with catalysts and saturated Ag/AgCl

electrode were used as the working and reference electrode respectively and placed in the cathodic compartment. A Pt gauze was used as the counter electrode and placed in the anodic compartment. Each compartment contained 30 mL electrolyte (0.5 M $KHCO_3$), leaving a headspace of 25 mL. All the potential readings were *i*R-corrected, and converted to the RHE scale ($E_{RHE} = E_{Ag/AgCl} + 0.1981$ V + 0.0591 V × pH – i × R), and R is obtained from electrochemical impedance spectroscopy. Cyclic voltammetry (CV) was performed at a scan rate of 10 mV s^{-1} controlled by CHI 660E potentiostate. For the electroreduction of Bi_2O_2Se NSs and Bi_2O_2Se NSs/OMC-N to Bi NSs and Bi NSs/OMC-N, the working electrode was biased at –1.4 V (*vs.* Ag/AgCl) for 2 hours. It was then quickly taken out from the electrolyte, and rinsed with deionized water for characterizations as described in the main text. For the contrast, the working electrodes of commercial Bi nanoparticles, Super P, and OMC-N were prepared under similar conditions with the loading mass of 1.0 mg cm^{-2}.

Catalyst characterization

Elemental analysis (EA) was performed using an Elementar Vario EL CUBE (Germany) instrument to determine the carbon, nitrogen, hydrogen, and oxygen contents of the samples. The Brunauer-Emmett-Teller test (BET) was collected by nitrogen adsorption and desorption tests using ASAP 2010 rapid specific surface and pore size distribution equipment (Micromeritics, USA). Sample degassing was carried out at 573 K prior to acquiring the adsorption isotherm. X-ray diffraction (XRD) patterns were collected on a Bruker D8 Focus X-ray diffractometer equipped with a monochromatized source of Cu Kα radiation (λ= 0.15406 nm) at 1.6 kW (40 kV, 40 mA). The patterns were recorded in a slow-scanning mode with 2θ from 10° to 80° with a scan-rate of 6° min^{-1}. The morphological characterizations were conducted with Carl Zeiss Sigma 500 field emission scanning electron microscopy (SEM). The elemental mapping was performed by energy–dispersive X–ray spectroscopy (EDS) attached to the SEM at 15 kV. Low and high resolution transmission electron microscopy (TEM) images were taken on a JEOL JEM-2100F TEM at an accelerating voltage of 200 kV equipped with an EDX unit (Si(Li) detector). The HAADF-STEM and EDX maps were performed on the JEM-2100F in STEM mode. Atomic force microscopy (AFM) images were taken using an atomic force microscopy (AFM, Bruker Dimension Icon) to characterize the microstructure of the samples. X-ray photoelectron spectroscopy (XPS) data were recorded with an Axis Ultra imaging photoelectron spectrometer (Kratos Analytical Ltd.) equipped with a hemispherical electron energy analyzer. The spectrometer was operated at 15 kV and 15 mA, and the Al Kα anode was used. The C 1*s* line (284.8 eV) was used as the reference to calibrate the binding energies (BE). Thermogravimetric analysis (TGA, TA SDT Q600) were performed from 20 to 800 ℃ at a heating/cooling rate of 10 ℃ min^{-1} in air to characterize the thermophysical properties.

CO_2RR measurements using H-cell configuration

The slurry was drop-casted onto a carbon fiber paper with loading mass of 1.0 mg cm^{-2} and naturally dried. The working electrode modified with catalysts and the reference electrode (saturated Ag/AgCl electrode) were placed in the cathodic compartment. The counter electrode (graphite rod) was placed in the anodic compartment. Two compartments were separated by a piece of Nafion-117 proton exchange membrane as the separator. Each compartment contained ~30 mL electrolyte (0.5 M $KHCO_3$), leaving a headspace of 25 mL. The electrolyte was pre-saturated with N_2 (pH = 8.4) or CO_2 (pH = 7.4). For CO_2RR electrocatalysis on Bi NSs, Bi NSs/OMC-N, commercial Bi nanopowder, and OMC-N, a flow of 20 sccm of CO_2 or N_2 was continuously bubbled into the electrolyte to maintain its

saturation. Cyclic voltammetry and polarization curves were carried out at a scan rate of 50 mV s^{-1} and 10 mV s^{-1}, respectively. All the potential readings were *i*R-corrected unless otherwise specified.

Full-cell CO_2 electrolysis measurements

For the full-cell measurements, 20 *wt.*% Ir/C (from Fuel Cell Store) was used as the oxygen evolution reaction (OER) electrocatalyst and similarly loaded onto 1 × 1 cm^2 carbon fiber paper to achieve areal loading of 1.0 mg cm^{-2}. The OER electrochemical performance of Ir/C catalyst was performed in the 0.5 M $KHCO_3$ and 1 M KOH. CO_2RR-OER electrolysis was performed in the same two-compartment H-cell configuration controlled by the electrochemical workstation or powered by two AA-sized alkaline batteries. All electrochemical results for this part were *i*R-compensated. Apart from the conventional power supply, overall CO_2/H_2O splitting electrolysis cell was powered by a commercial polysilicon multi-junction solar cell. Voltage between two electrodes was measured by voltmeter and current through the circuit was measured by amperemeter.

Flow cell measurements

Flow cell measurements were performed in a custom-designed flow cell reactor made of polytetrafluoroethylene plastic. It consists of two parts, which is GDE-loading Bi NSs or Bi NSs/OMC-N electrocatalysts (1.0 mg cm^{-2}, 1.5×3.5 cm^2) as the cathode, a GDE-loading 20 *wt.*% Ir/C (1.0 mg cm^{-2}, 1.5×3.5 cm^2) as the anode and a piece of anion exchange membrane (SELEMION, 1.5 × 3.5 cm^2) as the separator. The cathode and anode compartments are 4 cm^3 each in volume. Ag/AgCl reference electrode was located inside the cathode compartment. During the measurements, CO_2 gas was directly fed to the cathode GDE at a rate of 80 sccm. The catholyte was 1 M KOH, which was forced to continuously circulate through the cathode compartment at a rate of 10 sccm.

Product analysis

In order to analyze the products and their Faradaic efficiency, electrolysis was conducted at a few selected potentials for 1 to 2 hours. During the electrolysis, the gas products from the cathode compartment were continuously vented into a gas chromatograph (GC, PANNA A91PLUS) equipped with a packed bed column (HaySep D) operated at 80 ℃ with a thermal conductivity detector and a flame ionization detector. Argon (Air liquid 5.0) was employed as carrier gas with a flow rate of 30 mL min^{-1}. The gaseous products H_2 and CO were separated in a molecular sieve column (Alltech, part no. 57732, 3.0 m×1/8 inch, molecular sieve 13X, 60/80 mesh) and hydrocarbons in a HaySep column (Alltech, part no. 14487, 2.0 m×1/8 inch, HaySep Q, 80/100 mesh). The concentration of H_2 was analyzed by a thermal conductivity detector (TCD), and the concentration of CO was analyzed by a flame ionization detector (FID) with a methanizer. The concentration of gaseous products was quantified by the integral area ratio of the reduction products to standards. Their Faradaic efficiencies were calculated as below:

$$FE_{gaseous\ product}(\%) = \frac{Q_{CO\ or\ H_2}}{Q_{total}} \times 100\% = \frac{(\frac{v}{60\ s/min}) \times (\frac{x}{24000\ cm^3/mol}) \times N \times F}{j} \times 100\%$$

where v (=20 sccm) is the flow rate of CO_2, x is the measured concentration of product in 0.5 mL sample loop based on the calibration of the GC with a standard gas, N (=2) is the number of electrons

required to form a molecule of CO or H_2, F is the Faraday constant (96500 C mol^{-1}), and j is the recorded current.

The liquid products were collected at the conclusion of each electrocatalysis and analyzed by ^1H NMR (Bruker AVIII HD 600). For the NMR, 0.5 ml of the catholyte was mixed with 0.1 ml of D_2O and 0.2 ml of 3-(Trimethylsilyl)-1-propanesulfonic acid sodium (DSS, as the internal standard). The concentrations of formate and methanol were quantitatively determined from their NMR peak areas relative to that of the internal standard using the calibration curve from a series of standard HCOONa and CH_3OH solutions. The Faradaic efficiency of liquid product was calculated as follows:

$$FE_{liquid\ product}(\%) = \frac{Q_{HCOO^-\ or\ CH_3OH}}{Q_{total}} \times 100\% = \frac{n_{HCOO^-\ or\ CH_3OH} \times N \times F}{j \times t} \times 100\%$$

where $n_{HCOO^-\ or\ CH3OH}$ is the measured amount of formate or methanol in the cathodic compartment, N is the number of electrons required to form a molecule of $HCOO^-$ (N=2) or CH_3OH (N=6), F is the Faraday constant (96500 C mol^{-1}), t is the reaction time, and j is the recorded current. Reaction time for liquid product detection was chosen 10 to 15 min, which is general procedure in the literatures. Formate and methanol partial current densities at different potentials were calculated by multiplying the overall geometric current density and their corresponding Faradaic efficiency.

The calculation of turnover frequency

The turnover frequency (TOF, s^{-1}) was calculated as follows:

$$\mathrm{TOF} = \frac{i \times E_F}{N \times F \times n_{tot}}$$

where i is the current, E_F is the Faradaic efficiency for the desired product, N is the number of electrons in the half reaction (N = 2 or 6 for CO_2 to $COOH^{-1}$ or CH_3OH conversion, respectively), F is the Faraday constant (F = 96485 C mol^{-1} electrons), and n_{tot} is the total moles of catalyst employed in the electrolysis. The TOF is calculated on the basis of the actually catalytic activity.

Electrochemical reduction of CO_2 to C_1 products

In order to synthesizes the methyl formate, high concentrations of formic acid and methanol are necessary. To prove that, we dropped the ink of Bi_2O_2Se/OMC-N (5 mg mL^{-1}) on carbon fiber paper (areal loading mass of 1 mg cm^{-2}) and naturally dried. The working electrode modified with catalysts and the reference electrode (saturated Ag/AgCl electrode) were placed in the cathodic compartment. The counter electrode (graphite rod) was placed in the anodic compartment. Two compartments were separated by a piece of Nafion-117 proton exchange membrane as the separator. Each compartment contained 50 mL electrolyte (0.5 M $KHCO_3$), which was pre-saturated with N_2 over 30 min. After electroreduction of Bi_2O_2Se/OMC-N to Bi NSs/OMC-N at −1.4 V (*vs.* Ag/AgCl) for 2 hours, the CO_2RR electrocatalysis was conducted with a flow of 20 sccm of CO_2 continuously bubbled into the electrolyte to maintain its saturation. Chronoamperometry curve was carried out at the potential of −1.4 V (*vs.* Ag/AgCl) over 24 hours. Thus, the high concentration of electroreduction catholyte was obtained, which was quantitatively characterized by ^1H NMR data.

After dehydration of electroreduction catholyte by adding the excess anhydrous sodium sulfate overnight, it was purified to the methanol and formic acid by the rotary evaporation. Before the operation, sulfuric acid was added into the electrolyte to neutralize the potassium bicarbonate and transfer the formate to formic acid. Under the vacuum, the rotation speed was set at 60 rpm. Two separate C_1 products were obtain using temperature-controlled evaporation. At the first stage of 50 to 55 °C, the first cut fraction was obtained, which was mainly methanol. After warning up to 75 to 80 °C, the second cut fraction was received which was mainly formic acid.

Theoretical calculations

The first-principles calculations are carried out by density functional theory (DFT) implanted in the Vienna ab initio simulation program package (VASP).[1,2] Perdew-Burke-Ernzerhof (PBE) functional is employed for the exchange-correlation term based on the generalized gradient approximation (GGA).[3] The projector augmented wave (PAW) method has been used to represent the atomic cores. The energy cutoff is set at 500 eV for the plane-wave basis, which yields total energies converged at least 0.001 eV per atom, as confirmed by calculations with higher cutoffs. The convergence criterion of the self-consistency process is set to 10^{-6} eV between two electronic steps. The Brillouin zone was sampled by the Monk-horst Pack scheme with a Γ-centered grid of 4×4×1 k point for the supercell. A vacuum space of 20 Å is added to avoid interactions between adjacent images. The structures are fully relaxed until the residual force is less than 0.001 eV/Å on each atom. The vdW interaction is corrected by DFT-D3 approach.[4]

In the text, we adopted the typical two-dimensional graphene to model the substrate such as pyridine, pyrrole, and graphite of carbon matrix, and a (4×4) supercell is used. To explore the activity of these catalysts, the absorbability of molecular CO_2 and its intermediate states at substrates are investigated, which can be denoted by adsorption energy, expressed as

$$\Delta E_{ad} = \Delta E_{total} - \Delta E_{sub} - \Delta E_{mol}$$

where E_{total} and E_{sub} are the total energy of the substrate with and without adsorption of the molecule, and E_{mol} is the energy of the free molecule in vacuum. Within the computational hydrogen electrode (CHE) model, the chemical potential of a proton-electron pair is equal to that of half a H_2 gas molecule. Furthermore, in order to know the thermodynamic behavior of the CO_2 reduction process, the Gibbs free energy of formation for each elementary step of CO_2 reduction is computed as

$$\Delta G_{ad} = \Delta E_{DFT} + \Delta E_{ZPE} - T\Delta S$$

where ΔE_{DFT}, ΔE_{ZPE} and ΔS are the differences in DFT total energy, zero-point energy, and entropy of the two states before and after reaction, respectively; temperature T is set to 298 K. Standard ideal gas methods were employed to compute E_{ZPE} and TS from temperature, pressure and the calculated vibrational energies. For adsorbates, all $3N$ degrees of freedom were treated as frustrated harmonic vibrations with negligible contributions from the catalysts' surfaces.

Table S1. The Bi_2O_2Se nanosheets under different synthesis conditions.

Sample	Synthesis temperature (℃)	Synthesis time (h)
80-1d	80	24
120-1h	120	1
120-2h	120	2
120-1d	120	24
120-3d	120	72
160-3d	160	72
200-3d	200	72
220-3d	220	72

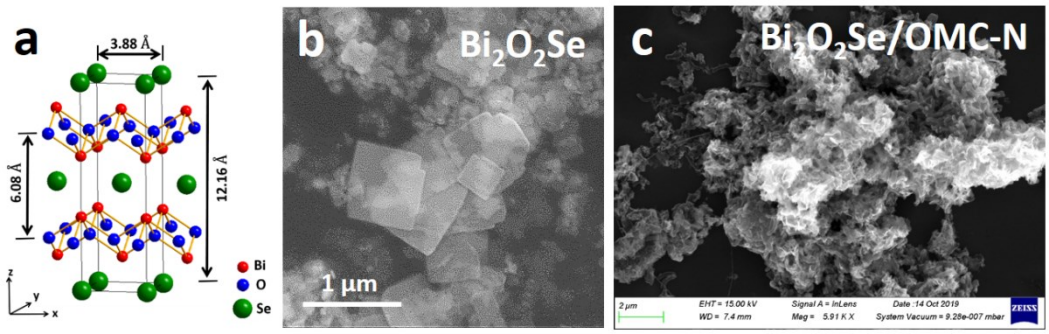

Figure S1. Structural characterizations of layered Bi_2O_2Se and Bi_2O_2Se/OMC-N composite. (**a**) schematic crystal structure of Bi_2O_2Se; (**b**) SEM image of Bi_2O_2Se; (**c**) SEM image of Bi_2O_2Se/OMC-N.

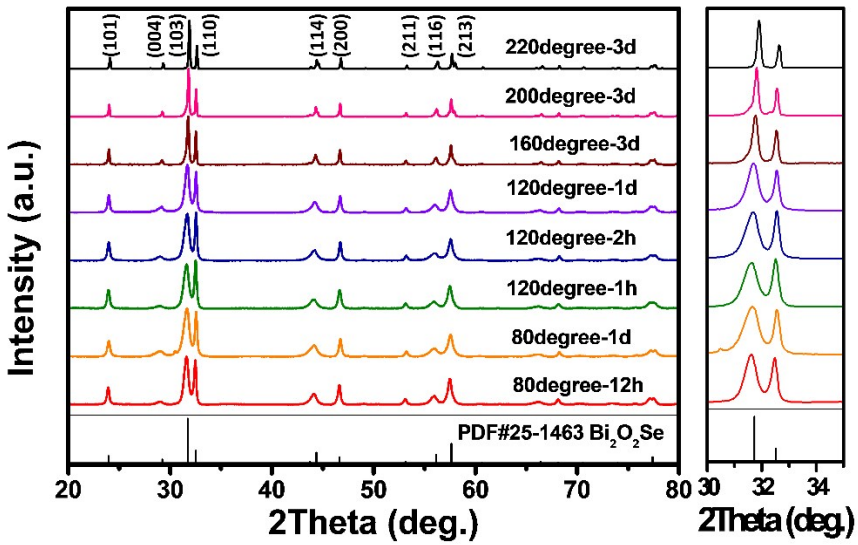

Figure S2. Powder X-ray diffraction patterns of Bi_2O_2Se nanosheets synthesized under different

conditions.

The average particle size of the Bi_2O_2Se nanosheets can be calculated by using the Scherrer equation:

$$D = \frac{K\lambda_{K_{\alpha 1}}}{B_{2\theta}\cos\theta}$$

In this equation, D is the average thickness of grain perpendicular to the grain plane, $\lambda_{K\alpha 1}$ is the X-ray wavelength ($\lambda_{K\alpha 1}$ =1.54056 Å), K is Scherrer constant. B is the half height width of the diffraction peak of the measured sample (double line correction and instrument factor correction were carried out). K is 0.89. θ is the Bragg diffraction angle of measured sample. The XRD patterns are noisy in appearance due to the presence of carbon support. To get a more accurate value of Bi_2O_2Se particle size, these patterns had been smoothed using Gaussian Fitting before the average particle sizes of Bi_2O_2Se were calculated based on the Scherrer equation.[5]

Table S2. The calculated grain size of Bi_2O_2Se nanosheets synthesized under different conditions.

Sample	Synthesis temperature (℃)	Synthesis time (hour)	The grain size calculated by XRD data (nm)	The grain size of (004) plane calculated by XRD data (nm)
80-12h	80	12	20.7	12.7
80-1d	80	24	26.5	7.9
120-1h	120	1	18.5	9.9
120-2h	120	2	27.7	11.9
120-1d	120	24	32.5	12.9
160-3d	160	72	60.6	34.3
200-3d	200	72	80.3	53.5
220-3d	220	72	90.3	58.2

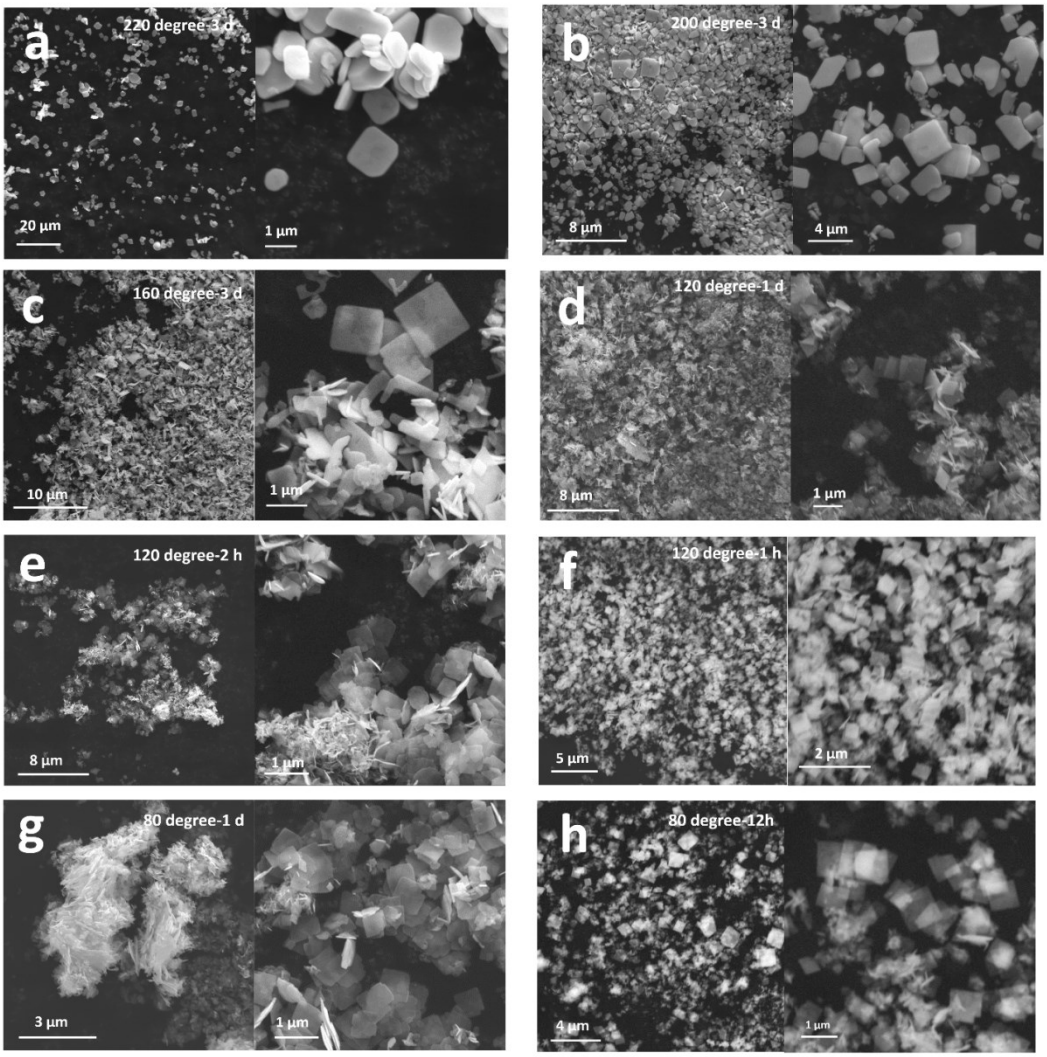

Figure S3. SEM images of Bi_2O_2Se nanosheets synthesized under different conditions. All conditions are described in the Experimental Methods section.

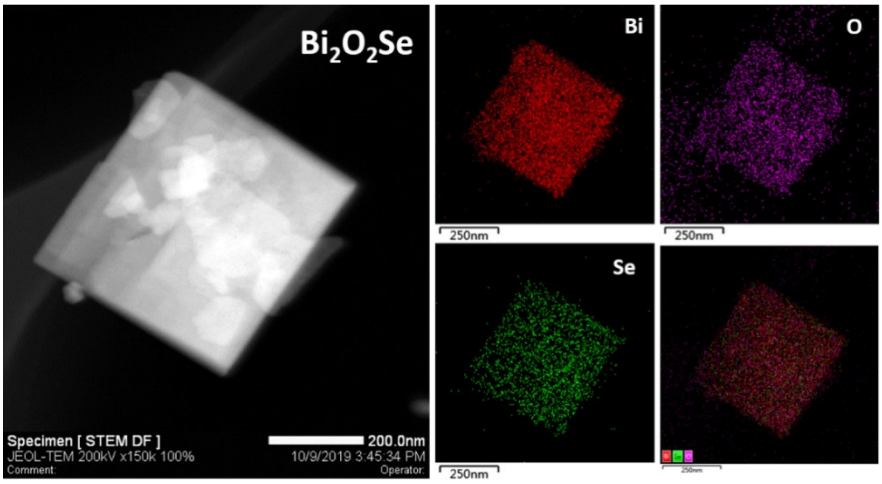

Figure S4. High angle annular dark field (HAADF) image of Bi_2O_2Se nanosheets, and the

corresponding elements distribution of Bi, Se, and O.

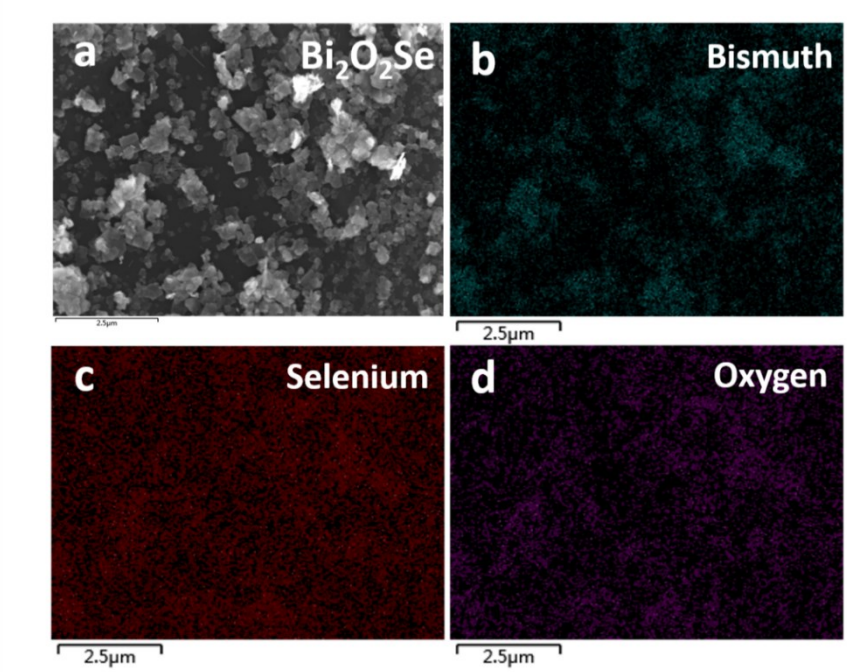

Figure S5. Element distribution of Bi_2O_2Se characterized by SEM-EDX. (**a**) SEM image of Bi_2O_2Se nanosheets; Elements distribution of Bi (**b**), Se (**c**), and O (**d**) measured by EDX.

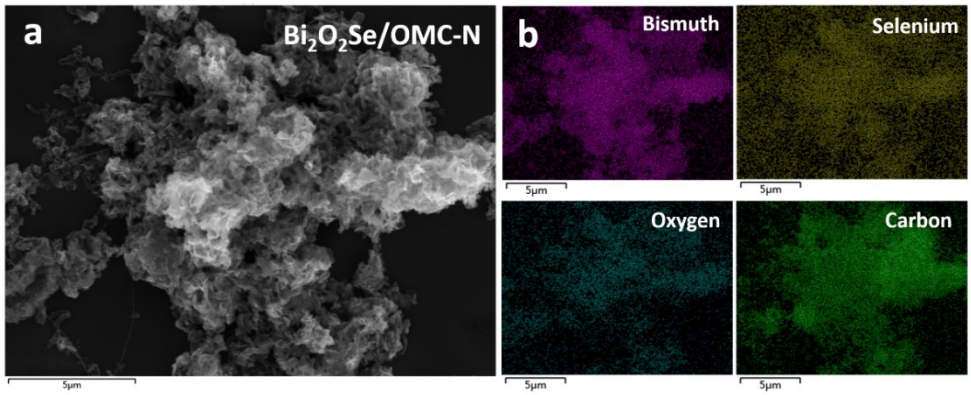

Figure S6. (**a**) SEM image of Bi_2O_2Se nanosheets grown on the OMC-N; (**b**) Elements distribution of Bi, Se, O, and C measured by EDX.

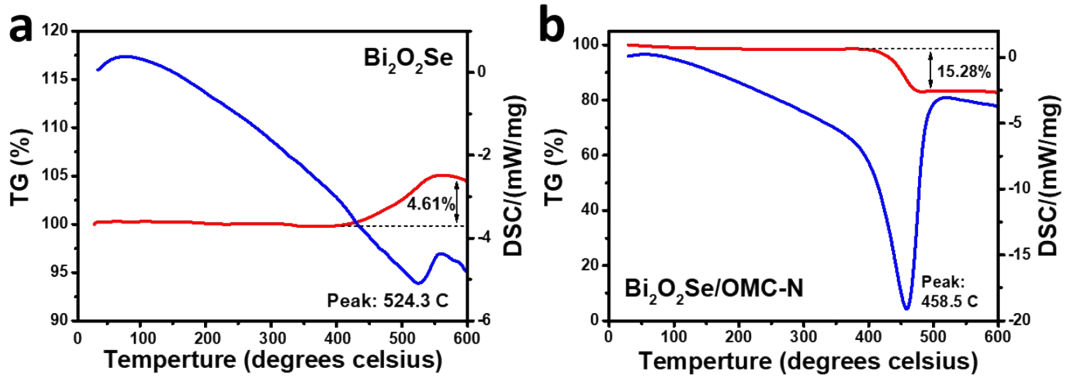

Figure S7. TGA and DSC analysis of Bi_2O_2Se NSs (**a**) and Bi_2O_2Se NSs/OMC-N (**b**) in air.

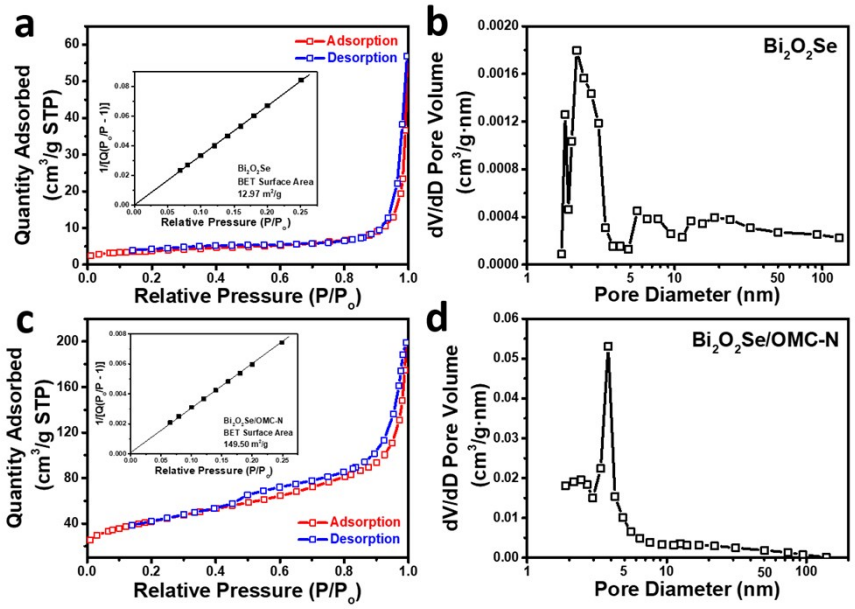

Figure S8. N_2 adsorption/desorption isotherms and pore size distribution of Bi_2O_2Se NSs and Bi_2O_2Se NSs/OMC-N. N_2 adsorption/desorption isotherms for Bi_2O_2Se NSs (**a**) and Bi_2O_2Se NSs/OMC-N (**c**) at 73 K, insets are corresponding BET surface area plots; BJH pore size distribution analysis of Bi_2O_2Se NSs (**b**) and Bi_2O_2Se NSs/OMC-N (**d**).

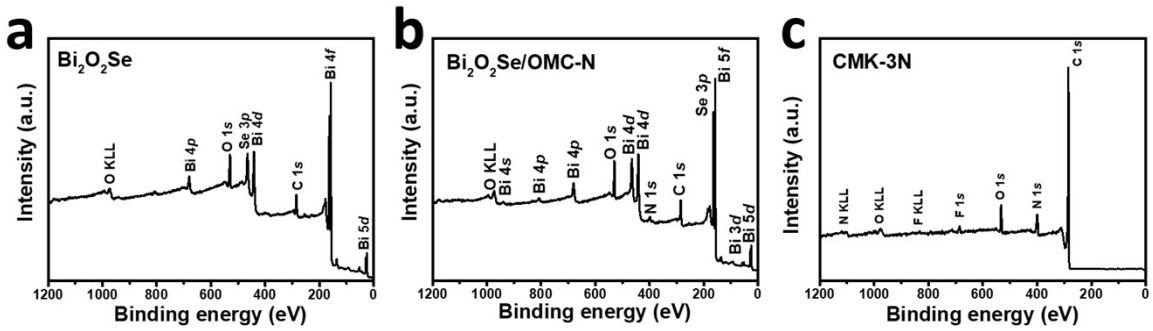

Figure S9. XPS spectra of the Bi_2O_2Se NSs (**a**), Bi_2O_2Se NSs/OMC-N (**b**), and OMC-N (**c**).

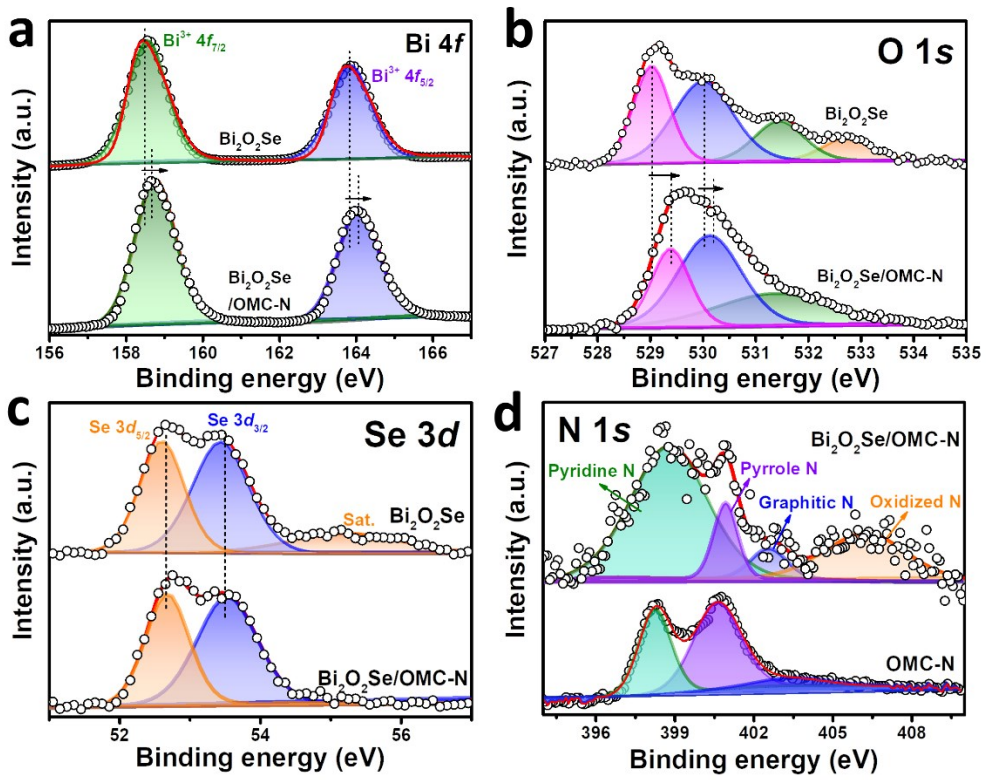

Figure S10. XPS spectra of Bi_2O_2Se NSs and Bi_2O_2Se NSs/OMC-N. (**a**) Bi 4*f* XPS spectra; (**b**) O 1*s* XPS spectra; (**c**) Se 3*d* XPS spectra of both materials; and (**d**) N 1*s* XPS spectra of Bi_2O_2Se NSs/OMC-N.

From the XPS results, it can be concluded that charge transfer from $[Bi_2O_2]^{2+}$ layer to carbon matrix occurs, leading to interaction between Bi_2O_2Se and the substrate. The first evidence is the shift to larger binding energy for Bi $4f_{7/2}$ or $4f_{5/2}$ peaks in Bi_2O_2Se/OMC-N composite than that of Bi_2O_2Se NSs (**Figure S10a**). It indicates that the electron density of Bi atom decreases and the charge transfer from Bi atom to carbon matrix. The second evidence is the red shift in the corresponding O 1*s* peaks of the composite. Besides, the two peaks of Se $3d_{5/2}$ and $3d_{3/2}$ are almost same as the two samples, which suggests that there is no valence state change of Se during the composition of Bi_2O_2Se and OMC-N.

Table S3. The ratio of different N configurations in Bi_2O_2Se/OMC-N and OMC/N.

Sample	Ratio of Pyridinic N (%)	Ratio of Pyrrolic N (%)	Ratio of Graphitic N (%)	Ratio of Oxidized N (%)
Bi_2O_2Se/OMC-N	59.49	10.87	6.54	23.10
OMC/N	37.48	55.17	7.35	/

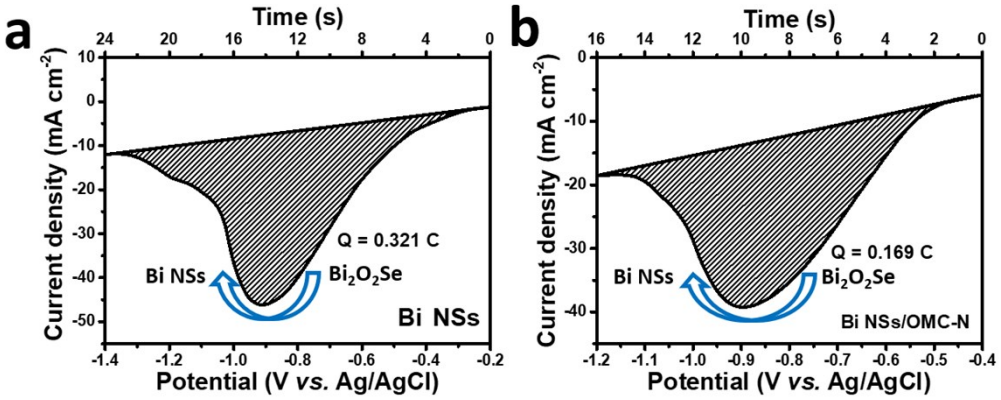

Figure S11. Total charge integrated from the Bi^{3+}/Bi^0 reduction peak for (**a**) Bi NSs and (**b**) Bi NSs/MOC-N. The CV data were collected in 0.5 M $KHCO_3$ at the scan rate of 50 mV s^{-1}. Using this value, we further estimated the percentage of surface Bi sites.

The calculation of surface Bi sites in Bi_2O_2Se and Bi_2O_2Se/OMC-N:

For the Bi NSs from the Bi_2O_2Se, the mole of Bi is 0.321 C / 96485 C mol^{-1} = 3.3269 × 10^{-6} mol; the number of Bi sites is 3.3269 × 10^{-6} mol × 6.02 × 10^{23} mol^{-6} = 2.003 × 10^{18}; the weight of reduced Bi is 3.3269 × 10^{-6} mol × 208.98 g mol^{-1} = 0.6953 mg; the percentage of reduced Bi to all the Bi_2O_2Se is 0.6953 mg / (5 mg /528.92 g mol^{-1} × 208.98 g mol^{-1}) × 100% = 35.19%;

For the Bi NSs from the Bi_2O_2Se/OMC-N, the mole of Bi is 0.169 C / 96485 C mol^{-1} = 1.7516 × 10^{-6} mol; the number of Bi sites is 1.7516 × 10^{-6} mol × 6.02 × 10^{23} mol^{-6} = 1.0544 × 10^{18} ; the weight of reduced Bi is 1.7516 × 10^{-6} mol × 208.98 g mol^{-1} = 0.366 mg; the percentage of reduced Bi to all the Bi_2O_2Se is 0.36604 mg / (5 mg × 80 % / 528.92 g mol^{-1} × 208.98 g mol^{-1}) × 100% = 23.16%;

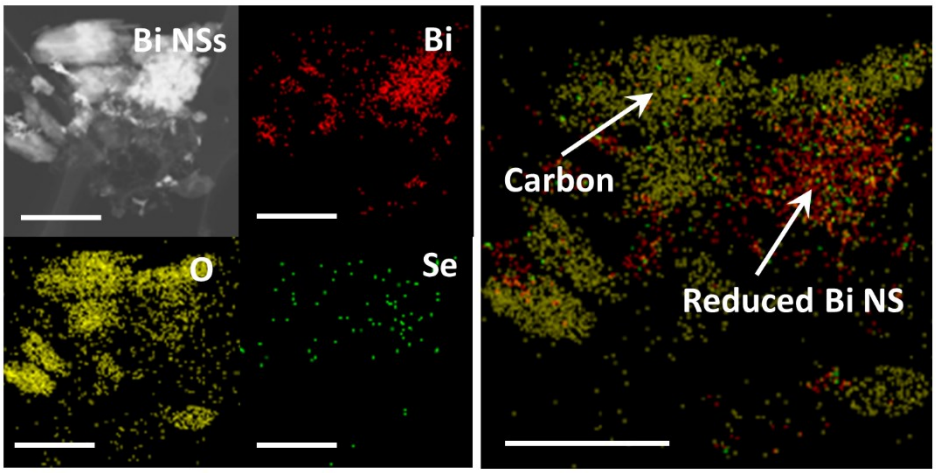

Figure S12. High angle annular dark field (HAADF) image of reduced Bi NSs, and the corresponding elements distribution of Bi, Se, and O. The bar is 1.2 μm.

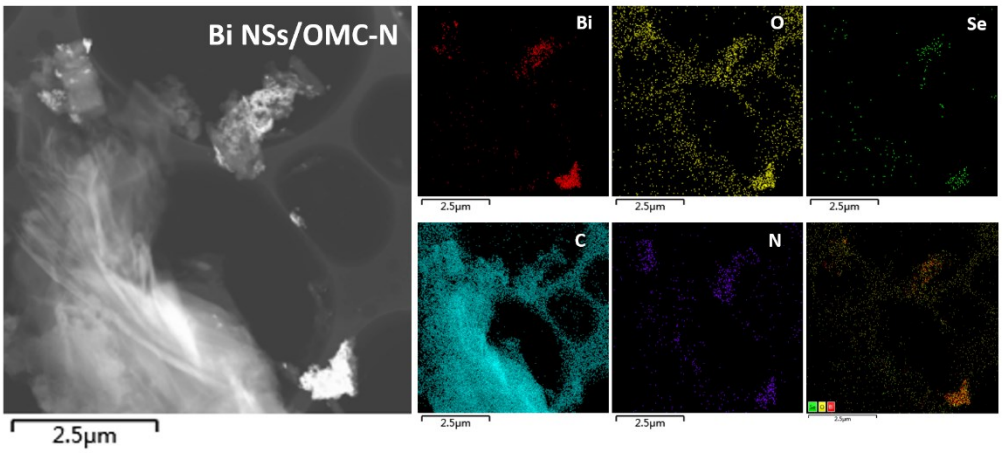

Figure S13. HAADF image of Bi NSs/OMC-N, and the corresponding elements distribution of Bi, Se, O, C, and N.

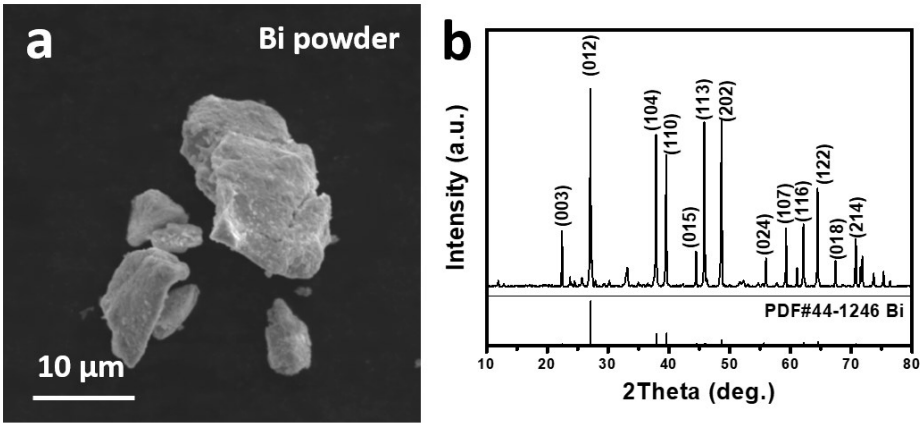

Figure S14. Structure characterizations of commercial Bi nanopowder. (**a**) SEM image and (**b**)

XRD pattern.

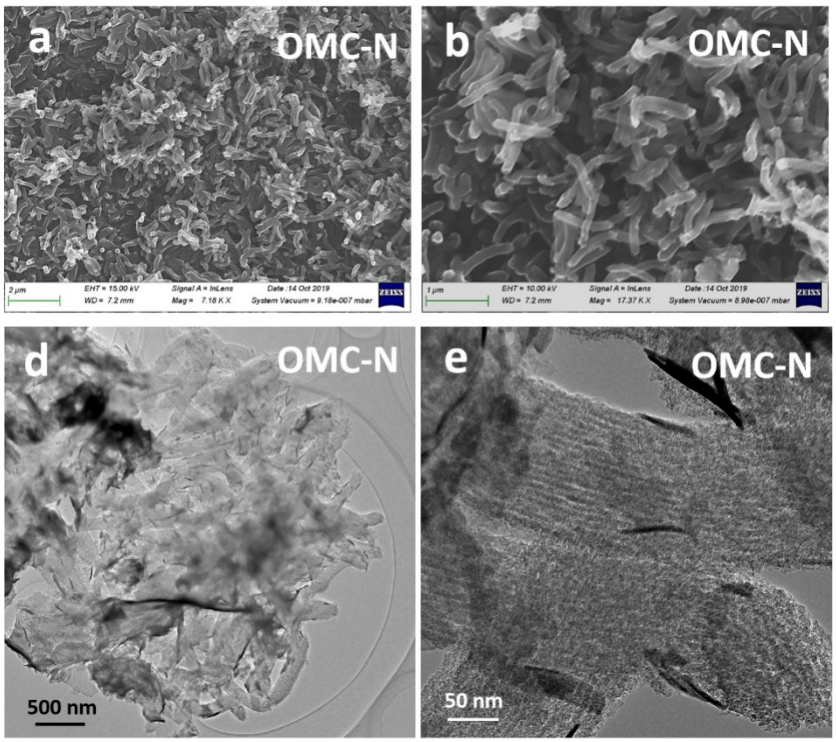

Figure S15. Morphology characterizations of nitrogen-doped ordered mesoporous carbon. (**a & b**) SEM images of OMC-N at different resolutions; (**c & d**) TEM images of OMC-N at different resolutions.

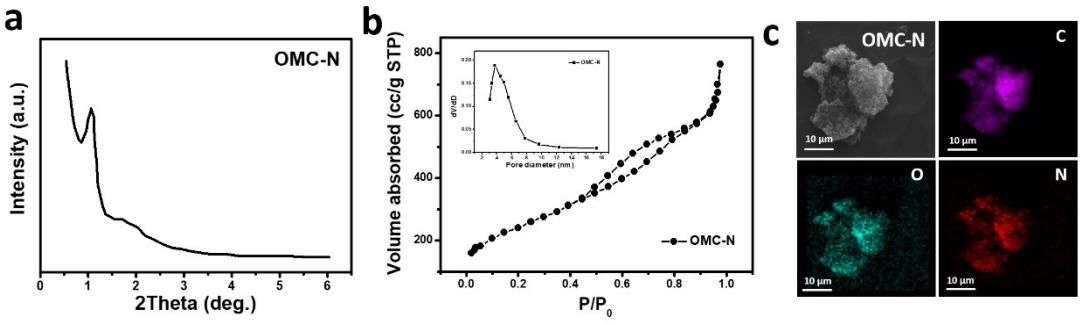

Figure S16. Structure characterizations of nitrogen-doped ordered mesoporous carbon. (**a**) Small angle X-ray diffraction (SAXRD) of OMC-N; (**b**) N_2 adsorption/desorption isotherms for OMC-N, the inset is its pore size distribution analysis; (**c**) SEM image of OMC-N and corresponding elements distribution of C, O, and N.

Table S4. The comparison of specific surface area and pore diameter of Bi_2O_2Se, Bi_2O_2Se/OMC-N, and OMC-N.

Sample	Specific surface area of BET ($m^2\ g^{-1}$)	Pore diameter (nm)
Bi_2O_2Se	12.96	1.8 and 2.2
Bi_2O_2Se/OMC-N	149.50	3.6
OMC-N	756.00	3.9

Table S5. The element ratio of OMC-N measured by EA and SEM-EDX.

Element	Atomic concentration (at. %) according to EA	Weight concentration (wt. %) according to EA	Atomic concentration (at. %) according to EDX	Weight concentration (wt. %) according to EDX
C	78.75	75.36	41.88	47.63
N	18.04	20.13	19.41	19.32
O	1.88	2.4	38.71	33.05
F	1.19	1.80	/	/
Si	0.14	0.30	/	/

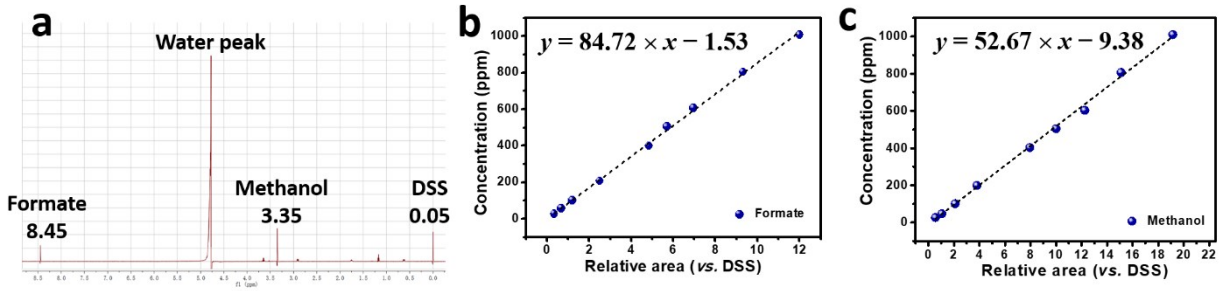

Figure S17. Identification of formate and methanol by ^{1}H NMR. (**a**) A typical NMR spectrum of the catholyte; Standard curve of formate by plotting the formate (**b**) and methanol (**c**) concentration with respect to the formate/DSS NMR peak area ratio.

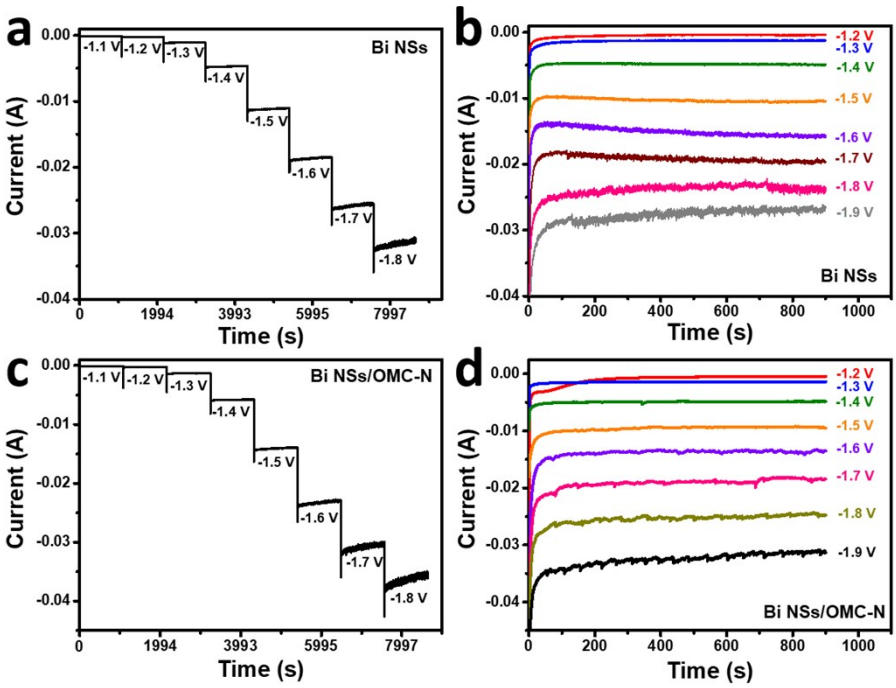

Figure S18. Chronoamperometric responses in CO_2-saturated electrolyte at different potentials for Bi NSs (**a**) and Bi NSs/OMC-N (**c**) during the gas phase product analysis; Chronoamperometric responses in CO_2-saturated electrolyte at different potentials as indicated for Bi NSs (**b**) and Bi NSs/OMC-N (**d**) during the liquid phase product analysis.

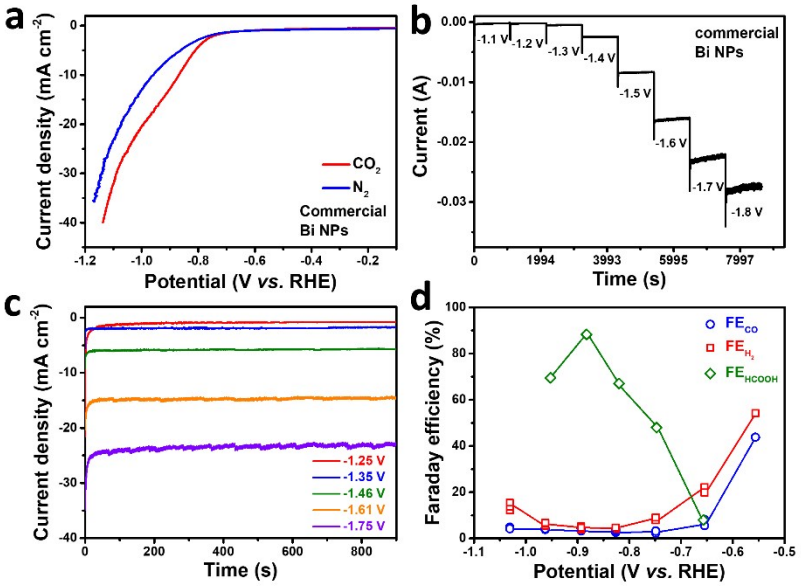

Figure S19. Electrocatalytic performance of commercial Bi nanopowder. (**a**) Polarization curves of commercial Bi nanopowders in N_2 or CO_2-saturated 0.5 M $NaHCO_3$; Chronoamperometric responses in CO_2-saturated electrolyte at different potentials during the gas phase product analysis (**b**) and liquid phase product analysis (**c**); (**d**) Faradaic efficiency of $HCOO^-$, H_2, and CO on commercial Bi nanopowders.

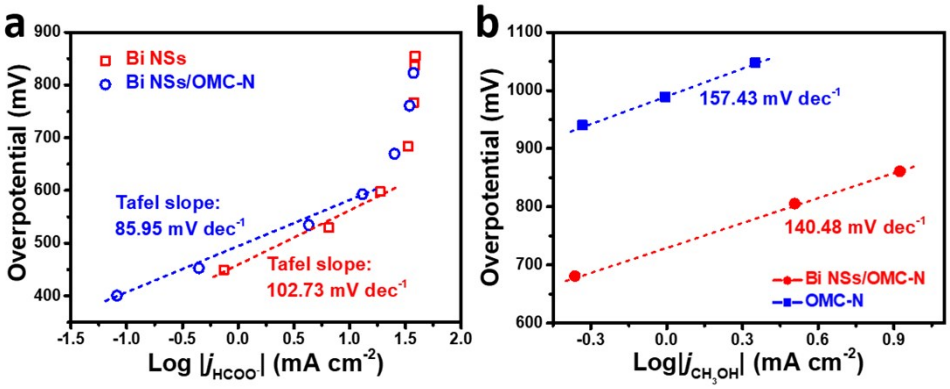

Figure S20. Tafel analysis of our Bi-based electrocatalysts. (**a**) Tafel plot of Bi NSs and Bi NSs/OMC-N for formate formation; (**b**) Tafel plot of Bi NSs/OMC-N and OMC-N for methanol formation.

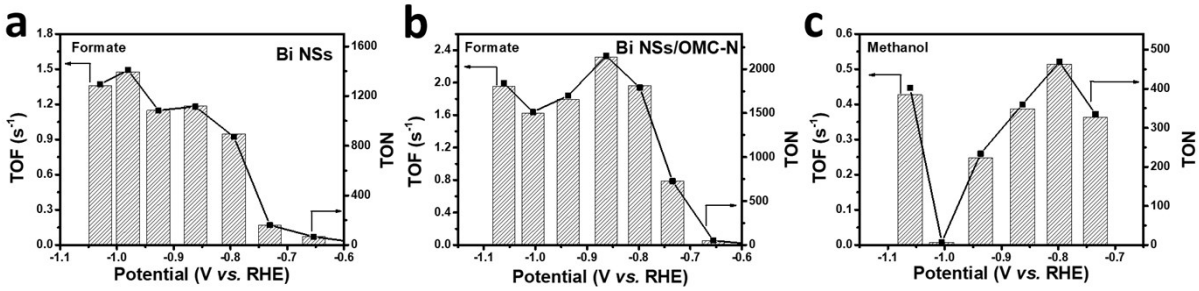

Figure S21. Electrocatalytic activity of electrocatalyst per active site. (**a**) TOF and TON of Bi NSs for formate production; (**b**) TOF and TON of Bi NSs/OMC-N for formate production; (**c**) TOF and TON of Bi NSs/OMC-N for methanol production.

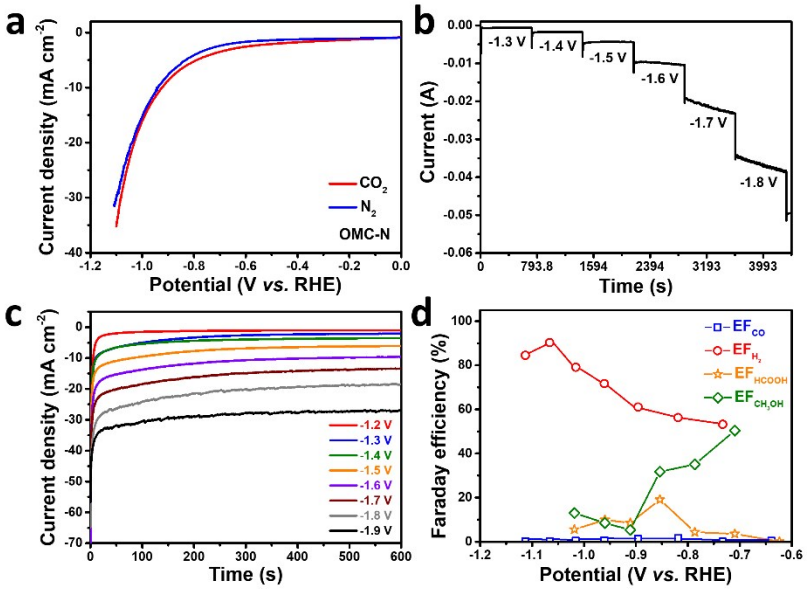

Figure S22. Electrocatalytic performance of nitrogen-doped ordered mesoporous carbon. (**a**) Polarization curves of OMC-N in N_2 or CO_2-saturated 0.5 M $NaHCO_3$; Chronoamperometric responses in CO_2-saturated electrolyte at different potentials during the gas phase product analysis (**b**) and liquid phase product analysis (**c**); (**d**) Faradaic efficiency of $HCOO^-$, H_2, and CO on OMC-N.

Table S6. Comparison of the performances of our Bi-based catalysts with other state-of-the-art electrocatalysts for formate formation in aqueous media.

Catalyst	Electrolyte	FE_{max}[a] (%)	$\eta_{max\ FE}$[b] (V)	$j_{formate}$[c] (mA cm^{-2})	Ref.
Bi NSs	**0.5 M $KHCO_3$**	**90**	**0.6823**	**31.64**	**This work**
Bi NSs/OMC-N		**71**	**0.670**	**25.43**	
Electrodeposited Sn	0.1 M $KHCO_3$	91.7	0.67	0.92	[6]
Graphene supported SnO_2 nanocrystals	0.1 M $NaHCO_3$	93.6	1.07	9.55	[7]
Electrodeposited Sn/SnO_2	0.5 M $NaHCO_3$	~40	0.61	0.72	[8]
Sn gas diffusion electrode	0.5 M $KHCO_3$	73.0	1.07	9.82	[9]
SnS_2 derived Sn on rGO	0.5 M $NaHCO_3$	84.5	0.68	11.75	[10]
Sn quantum sheets confined in graphene	0.1 M $NaHCO_3$	89	1.07	18.78	[11]
Porous Sn nanowires	0.1 M $KHCO_3$	78	0.91	~9.1	[12]
Core-shell Ag-Sn bimetallic nanoparticles	0.5 M $NaHCO_3$	87.2	0.81	~18	[13]
Hierarchical Bi dendrite	0.5 M $KHCO_3$	~89	0.65	2.4	[14]
Bi nanodendrites	0.5 M $NaHCO_3$	96.4	1.07	15.2	[15]
Liquid-phase exfoliated Bi nanosheets	0.1 M $KHCO_3$	86	0.90	16.5	[16]
defect-rich Bi derived from Bi_2S_3	0.5 M $NaHCO_3$	84.0	0.55	5.04	[17]

BiO_x/C nanoparticles	0.5 M $NaHCO_3$	93.4	0.65	16.1	[18]
Sb NS-G	0.5 M $NaHCO_3$	88.5	0.87	7.5	[19]
Nitrogen–doped graphene	0.5 M $KHCO_3$	73	0.75	5.48	[20]
Polyethylenimine-enhanced N-doped carbon nanotubes	0.1 M $KHCO_3$	87	1.07	8.27	[21]
nitrogen-doped nanoporous carbon/carbon nanotube composite	0.1 M $KHCO_3$	81	0.9	~3.2	[22]

[a] The maximum faradaic efficiency for formate formation.

[b] Overpotential at FE_{max}, calculated with respect to the formal potentials.

[c] Partial current density for formate at FE_{max}.

Table S7. Comparison of the performances of Bi NSs/OMC-N with other state-of-the-art electrocatalysts for methanol formation in aqueous media.

Catalyst	**Electrolyte**	**FE_{max} (%)**	**$E_{max\ FE}$**	**Ref.**
Bi NSs/OMC-N	0.5 M $KHCO_3$	67.3	−0.606 V *vs.* RHE	This work
Cu_2O electrodeposited-stainless steel	0.5 M $KHCO_3$	38	−0.443 V *vs.* RHE	[23]
Cu/CuO nanopowder painted carbon GDE	1 M $KHCO_3$	2.5	−0.743 V *vs.* RHE	[24]
Cu_2O-MWCNTs	0.5 M $KHCO_3$	38	−0.8 V *vs.* Ag/AgCl	[25]
Cu_2O/ZnO-based electrodes	0.5 M $KHCO_3$	17.7	−1.3 V *vs.* Ag/AgCl	[26]
Cu-Au alloy	0.5 M $KHCO_3$	15.9	−1.1 V *vs.* SCE	[27]
HKUST-1	0.5 M $KHCO_3$	5.6	−1.0 V *vs.* Ag/AgCl	[28]
Ru doped HKUST-1	0.5 M $KHCO_3$	47.2	−2.0 V *vs.* Ag/AgCl	[29]

CuSAs/TCNFs	0.1 M $KHCO_3$	44.0	−0.9 V *vs.* RHE	[30]
Boron-doped diamond	0.1 M NH_4HCO_3	24.3	−1.3 V *vs.* Ag/AgCl	[31]
Cu/CuO	1 M $KHCO_3$	2.5	−1.35 V *vs.* Ag/AgCl	[32]
CuO	0.5 M $KHCO_3$	28	−1.3 V *vs.* RHE	[33]
Cu_2O/ZnO	0.5 M $KHCO_3$	17.7	−1.3 V *vs.* Ag/AgCl	[34]

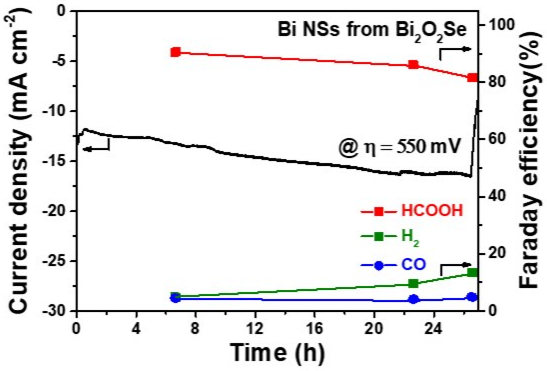

Figure S23. The Faraday efficiencies of formate, H_2, and CO for the Bi NSs at the overpotential of 550 mV.

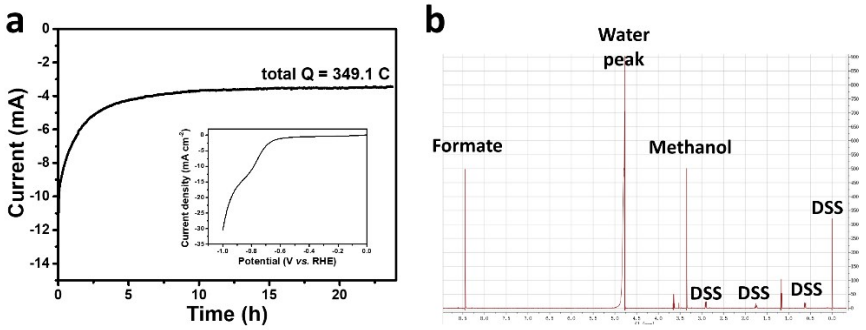

Figure S24. The long-term CO_2/H_2O splitting electrolysis. (**a**) chronoamperometry curve of Bi NSs/OMC-N||Ir/C for 24 hours, the inset is the corresponding LSV curve; (**b**) the ^1H NMR data of obtained catholyte.

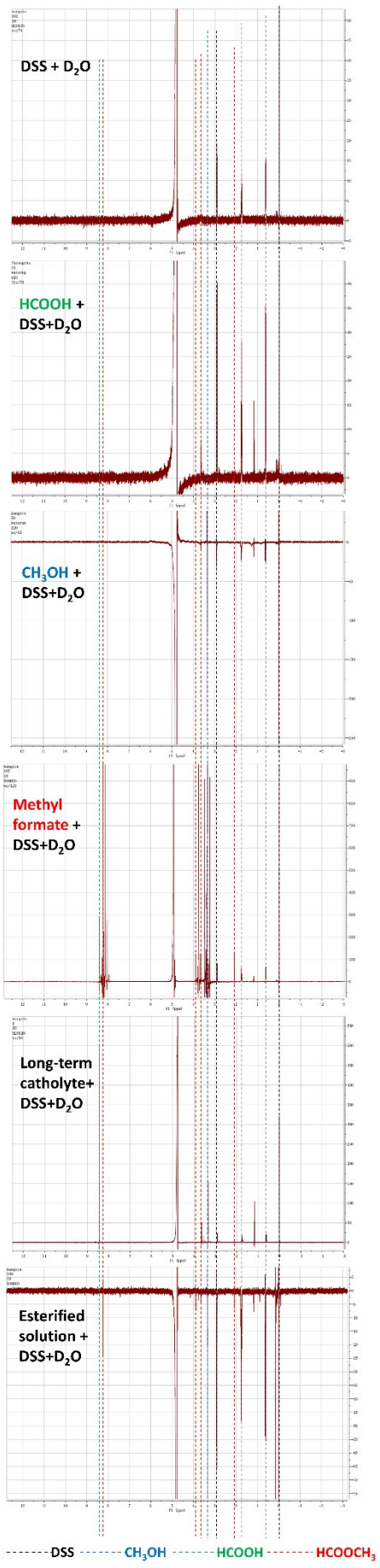
DSS + D2O
HCOOH + DSS+D2O
CH3OH + DSS+D2O
Methyl formate + DSS+D2O
Long-term catholyte+ DSS+D2O
Esterified solution + DSS+D2O
DSS
CH3OH
HCOOH
HCOOCH3

Figure S25. The ^{1}H NMR data of a series of samples, including blank catholyte, pure methanol, pure formic acid, pure methyl formate, long-term electrolysis catholyte, and esterified catholyte. Qualitative determination of different materials by peak position, such as DSS (as the internal standard, black dotted line), methanol (blue dotted line), formate or formic acid (green dotted line), and methyl formate (red dotted line). The peak located at 1.25 ppm can be rapidly assigned to ethanol impurity.

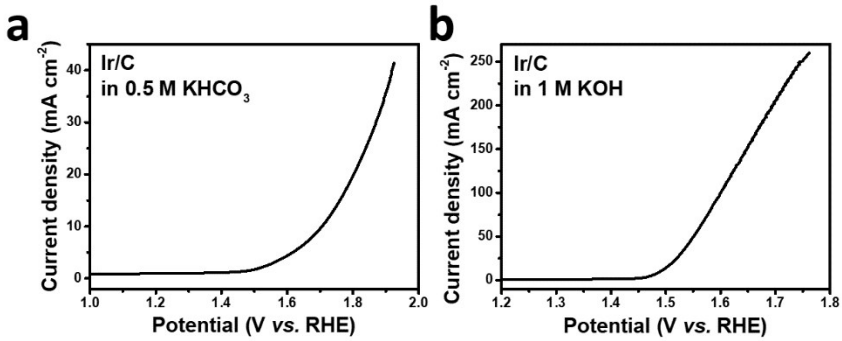

Figure S26. The oxygen evolution reaction (OER) performance of Ir/C in different electrolytes. (**a**) Polarization curve of Ir/C for OER electrocatalysts in 0.5 M $NaHCO_3$; (**b**) Polarization curve of Ir/C for OER electrocatalysts in 1 M KOH.

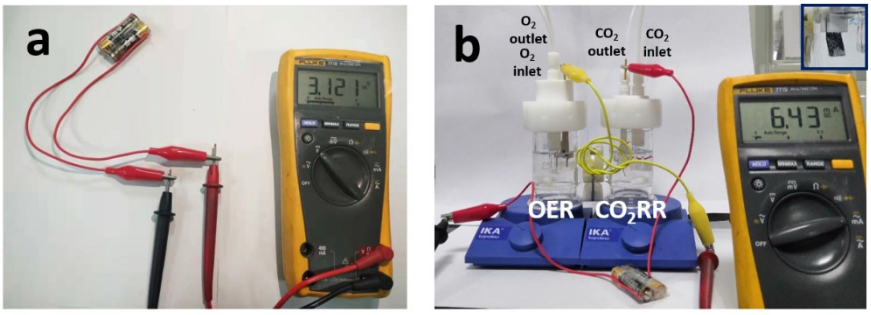

Figure S27. Full-cell electrolysis by coupling Bi NSs/OMC-N CO_2RR catalyst with Ir/C OER catalysts. Photograph of the setup for the CO_2RR-OER electrolysis powered by two AA-size alkaline batteries with the open circuit voltage of 3.12 V.

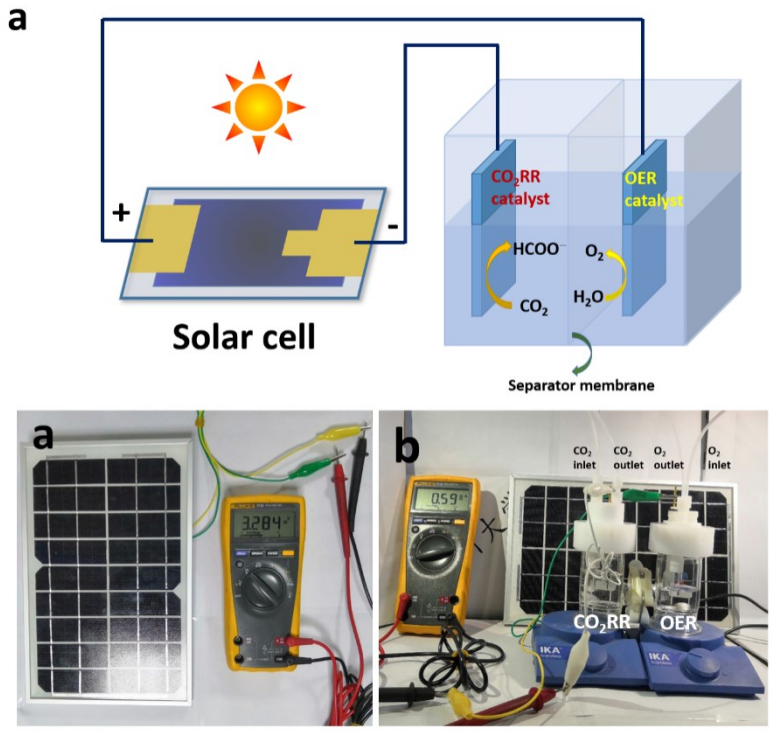

Figure S28. Full-cell electrolysis of Bi NSs/OMC-N||Ir/C driven by a polysilicon multijunction solar cell. (**a**) Schematic diagram of the experimental setup for the solar-driven full-cell electrolysis; (**b**) Photograph of the open circuit voltage by the commercial polysilicon multijunction solar cell under the fluorescent lamp; (**c**) Photograph of the setup for the CO_2RR-OER electrolysis powered by the solar cell under the fluorescent lamp.

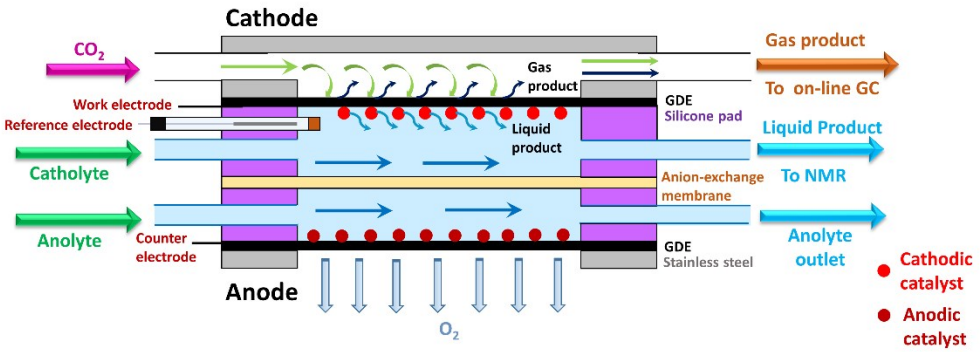

Figure S29. Schematic illustration of the three-electrode flow cell configuration.

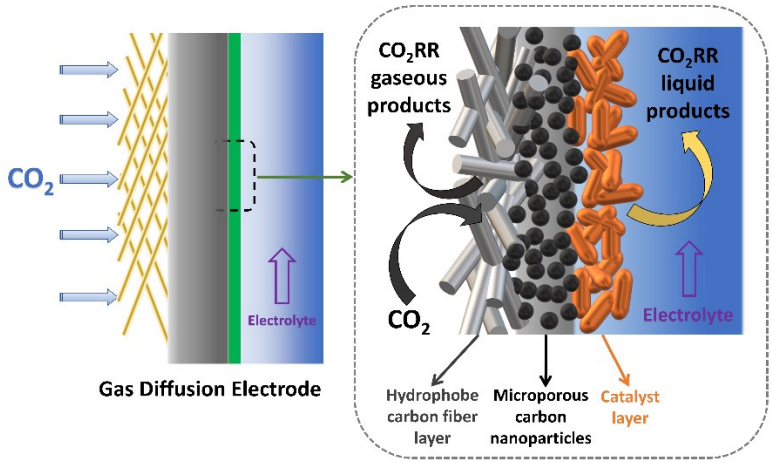

Figure S30. Schematic of the cathode portion of a gas diffusion electrode, and the structure of the electrode refers to the Sargent's work[35].

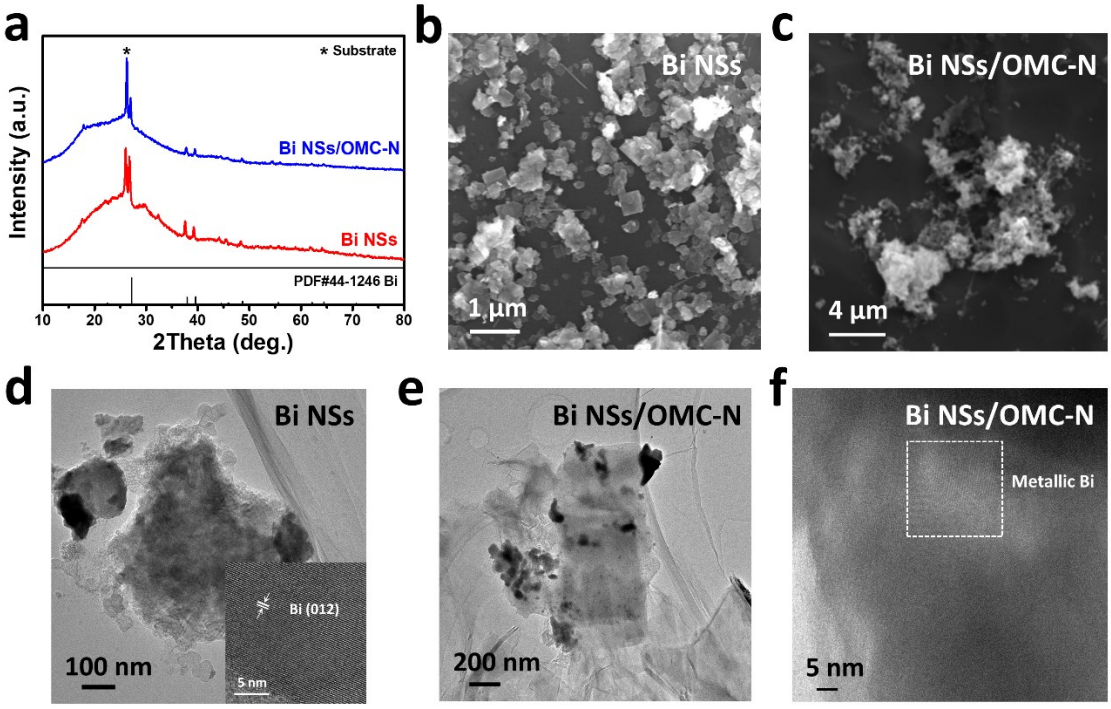

Figure S31. Postmortem characterizations of Bi NSs and Bi NSs/OMC-N after amperometric stability test. (a) XRD pattern and (**b & c**) SEM images of Bi NSs and Bi NSs/OMC-N; (**d-f**) TEM images of Bi NSs and Bi NSs/OMC-N.

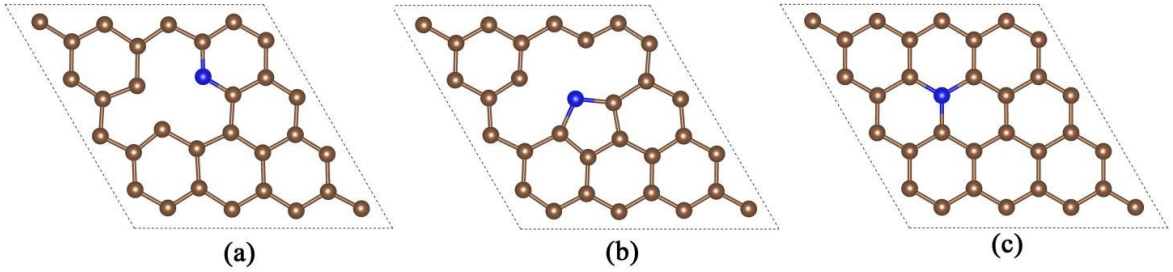

Figure S32. Optimized structures for N-doped carbon matrixes, which are used (4×4) graphene sheet as the substrate. The C atom is brown ball and N atom is blue ball.

Table S8. The adsorption energy ΔE (eV) of CO_2 molecule and CO_2 intermediates adsorbed at N-doped carbon matrix. The negative value means the molecule favors to be adsorbed at substrates.

ΔE (eV)	**CO_2**	***COOH**	***HCOOH**	***CHO**	***CHOH**	***CH_2OH**	***CH_3OH**
Pyridine	−0.195	−2.14	−0.23 −1.05 for *COHOH	−2.74	−2.37	−2.44	−0.345
Pyrrole	−0.197	−1.64	−0.221	−1.96	−5.32	−2.15	−0.184
Graphitic	−0.168	0.382	−0.202	−0.247	−0.501	−0.473	−0.210

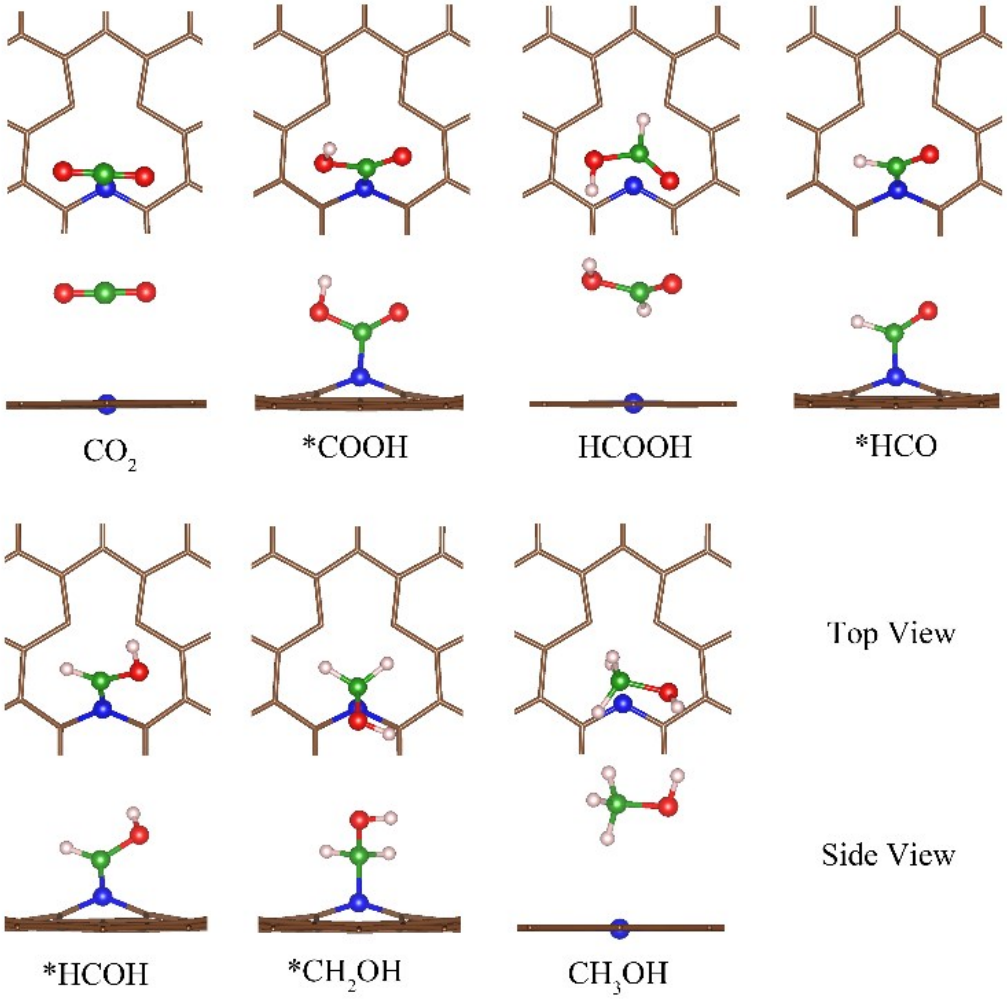

Figure S33. The relaxed intermediate structures during CO_2 reduction process. The top view of the CO_2 reduction is corresponding to the upper image, while the side view is denoted at the lower image. The C atom is brown ball, N is blue ball, O atom is red ball, and H atom is pink ball. It should be mentioned that C atom of CO_2 is green ball.

Reference

[1] G. Kresse and J. Hafner, *Phys. Rev. B*, 1993, 47, 558.

[2] G. K. a. J. Furthmuler, *Phys. Rev. B*, **1996**, 54, 11169.

[3] J. Heyd, G. E. Scuseria, and M. Ernzerhof, *J. Chem. Phys.*, **2006**, 124, 219906.

[4] S. Grimme, J. Antony, S. Ehrlich, and H. Krieg, *J. Chem. Phys.*, **2010**, 132, 1, 154104.

[5] S. Zhang, Y. Shao, G. Yin, Y. Lin, *J. Mater. Chem.*, **2009**,19, 7995–8001.

[6] C. Zhao, J. Wang, *Chem. Eng. J.,* **2016**, 293, 161–170.

[7] S. Zhang, P. Kang, T. J. Meyer, *J. Am. Chem. Soc.,* **2014**, 136, 5, 1734–1737.

[8] Y. Chen, M. W. Kanan, *J. Am. Chem. Soc.,* **2012**, 134, 4, 1986–1989.

[9] Q. Wang, H. Dong, H. Yu, *J. Power. Sourc.,* **2014**, 271, 278–284.

[10] F. Li, L. Chen, M. Xue, T. Williams, Y. Zhang, D. R. MacFarlane, J. Zhang, *Nano Energy,* **2017**, 31, 270–277.

[11] F. Lei, W. Liu, Y. Sun, J. Xu, K. Liu, L. Liang, T. Yao, B. Pan, S. Wei, Y. Xie, *Nat. Commun.,* **2016**, 7, 12697.

[12] B. Kumar, V. Atla, J. P. Brian, S. Kumari, T. Q. Nguyen, M. Sunkara, J. M. Spurgeon, *Angew. Chem. Int. Ed.,* **2017**, 56, 13, 3645–3649.

[13] W. Luc, C. Collins, S. Wang, H. Xin, K. He, Y. Kang, F. Jiao, *J. Am. Chem. Soc.,* **2017**, 139, 5, 1885–1893.

[14] J. H. Koh, D. H. Won, T. Eom, N.-K. Kim, K. D. Jung, H. Kim, Y. J. Hwang, B. K. Min, *ACS Catal.,* **2017**, 7, 8, 5071–5077.

[15] H. Zhong, Y. Qiu, T. Zhang, X. Li, H. Zhang, X. Chen, *J. Mater. Chem. A,* **2016**, 4, 13746–13753.

[16] W. Zhang, Y. Hu, L. Ma, G. Zhu, P. Zhao, X. Xue, R. Chen, S. Yang, J. Ma, J. Liu, Z. Jin, *Nano Energy,* **2018**, 53, 808–816.

[17] F. Li, M. Xue, J. Li, X. Ma, L. Chen, X. Zhang, D. R. MacFarlane, J. Zhang, *Angew. Chem. Int. Ed.,* **2017**, 129, 46, 14910–14914.

[18] Y. Zhang, F. W. Li, X. L. Zhang, T. Williams, C. D. Easton, A. M. Bond, J. Zhang, *J. Mater. Chem. A* **2018**, 6, 4714−4720.

[19] C. W. Lee, J. S. Hong, K. D. Yang, K. Jin, J. H. Lee, H.-Y. Ahn, H. Seo, N.-E. Sung, K. T. Nam, *ACS Catal.* **2018**, 8, 931−937.

[20] H. Wang, Y. Chen, X. Hou, C. Ma, T. Tan, *Green Chem.,* **2016**, 18, 3250–3256.

[21] S. Zhang, P. Kang, S. Ubnoske, M. K. Brennaman, N. Song, R. L. House, J. T. Glass, T. J. Meyer, *J. Am. Chem. Soc.,* **2014**, 136, 22, 7845–7848.

[22] H. Wang, J. Jia, P. Song, Q. Wang, D. Li, S. Min, C. Qian, L. Wang, Y. F. Li, C. Ma, T. Wu, J. Yuan, M. Antonietti, G. A. Ozin, *Angew. Chem. Int. Ed.,* **2017**, 56, 27, 7847–7852.

[23] M. Le, M. Ren, Z. Zhang, P.T. Sprunger, R.L. Kurtz, J.C. Flake, *J. Electrochem. Soc.,* **2011**, 158, 45–49.

[24] Y. Lan, S. Ma, J. Lu, P.J.A. Kenis, *Int. J. Electrochem. Sci.,* **2014**, 9, 7300–7308.

[25] M. I. Malik, Z. O. Malaibari, M. Atieh, B. Abussaud, *Chem. Eng. Sci.,* **2016**, 152, 468–477.

[26] J. Albo, A. Sáez, J. S Gullón, V. Montiel, A. Irabien, *Appl. Catal. B: Environ.,* **2015**, 176, 709–717.

[27] F. Jia, X. Yu, L. Zhang, *J. Power Sources* **2014**, 252, 85−89.

[28] J. Albo, D. Vallejo, G. Beobide, O. Castillo, P.Castaño, A. Irabien, *ChemSusChem* **2017**, 10, 1100−1109.

[29] M. Perfecto-Irigaray, J. Albo, G. Beobide, O. Castillo, A. Irabien, S. Pérez-Yáñez, *RSC Adv.* **2018**, 8, 21092−21099.

[30] H. Yang, Y. Wu, G. Li, Q. Lin, Q. Hu, Q. Zhang, J. Liu, C. He, *J. Am. Chem. Soc.* **2019**, 141, 12717−12723.

[31] P. K. Jiwanti, K. Natsui, K. Nakata, Y. Einaga, *RSC Adv.* **2016**, 6, 102214–102217.

[32] Y. Lan, S. Ma, J. Lu, P.J.A. Kenis, *Int. J. Electrochem. Sci.* **2014**, 9, 7300–7308.

[33] M. Le, M. Ren, Z. Zhang, P. T. Sprunger, R. L. Kurtz, J. C. Flake, *J. Electrochem. Soc.* **2011**, 158, 45–49.

[34] J. Albo, A. Saez, J. Solla-Gullon, V. Montiel, A. Irabien, *Appl. Catal. B Environ.* **2015**, 709, 176–177.

[35] C.-T. Dinh, T. Burdyny, M. G. Kibria, A. Seifitokaldani, C. M. Gabardo, F. P. G. de Arquer, A. Kiani, J. P. Edwards, P. D. Luna, O. S. Bushuyev, C. Zou, R. Q.-Bermudez, Y. Pang, D. Sinton, E. H. Sargent, *Science,* **2018**, 360, 783–787.